

3D Analysis of the Morphology and Spatial Distribution of Nitrogen in Nitrogen-Doped Carbon Nanotubes by Energy-Filtered Transmission Electron Microscopy Tomography

Ileana Florea,^{*,†} Ovidiu Ersen,[†] Raul Arenal,^{||,⊥,#} Dris Ihiawakrim,[†] Cédric Messaoudi,[§] Kambiz Chizari,[‡] Izabela Janowska,[‡] and Cuong Pham-Huu[‡]

[†]Institut de Physique et Chimie des Matériaux de Strasbourg (IPCMS), UMR 7504 CNRS, 23 rue du Loess, 67037 Strasbourg, France

[‡]Laboratoire des Matériaux, Surfaces et Procédés pour la Catalyse (LMSPC), UMR 7515 CNRS Université de Strasbourg, 25 rue Becquerel 67087 Strasbourg, France

[§]Institut Curie Paris, 26 rue d'Ulm 75248 Paris Cedex 05, France

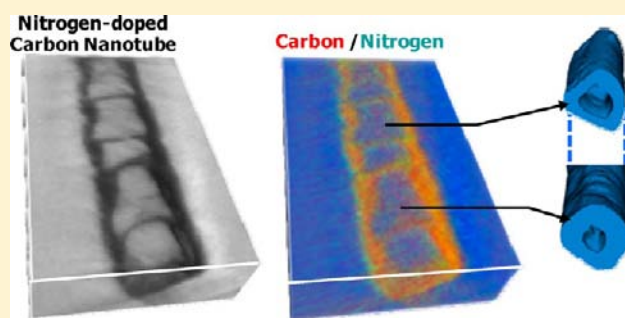
^{||}Laboratorio de Microscopias Avanzadas (LMA), Instituto de Nanociencia de Aragon (INA), Universidad de Zaragoza, 50018 Zaragoza, Spain

[⊥]Fundacion ARAID, 50004 Zaragoza, Spain

[#]Laboratoire d'Etude des Microstructures, CNRS - ONERA, 92322 Chatillon, France

Supporting Information

ABSTRACT: We present here the application of the energy-filtered transmission electron microscopy (EFTEM) in the tomographic mode to determine the precise 3D distribution of nitrogen within nitrogen-doped carbon nanotubes (N-CNTs). Several tilt series of energy-filtered images were acquired on the K ionization edges of carbon and nitrogen on a multiwalled N-CNT containing a high amount of nitrogen. Two tilt series of carbon and nitrogen 2D maps were then calculated from the corresponding energy-filtered images by using a proper extraction procedure of the chemical signals. Applying iterative reconstruction algorithms provided two spatially correlated C and N elemental-selective volumes, which were then simultaneously analyzed with the shape-sensitive reconstruction deduced from Zero-Loss recordings. With respect to the previous findings, crucial information obtained by analyzing the 3D chemical maps was that, among the two different kind of arches formed in these nanotubes (transversal or rounded ones depending on their morphology), the transversal arches contain more nitrogen than do the round ones. In addition, a detailed analysis of the shape-sensitive volume allowed the observation of an unexpected change in morphology along the tube axis: close to the round arches (with less N), the tube is roughly cylindrical, whereas near the transversal ones (with more N), its shape changes to a prism. This relatively new technique is very powerful in the material science because it combines the ability of the classical electron tomography to solve 3D structures and the chemical selectivity of the EFTEM imaging.



■ INTRODUCTION

The insertion of foreign elements into the hexagonal network of the carbon nanotube walls could lead to a significant modification of their intrinsic properties. Among the different doped carbon nanotubes, the nitrogen-doped carbon nanotubes (N-CNTs) have received an increasing scientific interest during the past decade due to the fact that nitrogen incorporation strongly modifies the chemical and physical properties of the pure carbon nanotubes.^{1–5} Despite the large amount of research effort, considerable progress is still needed to complete the understanding and optimization of their properties for downstream applications. For instance, in catalysis, these N-doped nanotubes could give rise to more interesting

applications as compared to the undoped ones, by either modifying the acido-basic properties or changing the electronic surface state of the support that modifies the interaction with the deposited active phase and thus generates a new catalytic system with better performance.^{6–8} Indeed, the presence of nitrogen atoms inside the carbon network structure seems to enhance the density of the anchorage sites for depositing metal or other active phase onto the nanotube surface. That leads to a higher dispersion of the active phase nanoparticles and thus to a significant improvement of the overall catalytic activity in the

Received: January 26, 2012

Published: May 22, 2012

case of liquid-phase hydrogenation as compared to the one obtained on the undoped CNT.⁹ Recently, Ma et al.¹⁰ and Feng et al.¹¹ suggest a new application of this material by demonstrating its ability to act as a metal-free catalyst for the oxygen reduction reaction (ORR) with high electrocatalytic performance and resistance toward deactivation. Pham-Huu and co-workers¹² have also reported the use of N-CNTs as metal-free catalyst for the selective oxidation of trace amount of H₂S into elemental sulfur at the reaction conditions close to those used in the industrial processes. The N-CNTs catalyst exhibits better catalytic performance as compared to that of the state-of-the-art Fe₂O₃/SiC and Fe₂O₃/SiO₂ catalysts and allows one to operate the reaction at higher reactant gaseous velocity and lower reaction temperature. The electronic state modification induced by the nitrogen incorporation seems to modify the adsorption mode of the oxygen, by inducing potential cross-linking adsorption positions (where the adsorbed atom bridges two atoms of the tube structure) instead of linear ones, which leads to a weakening of the O–O bond. However, despite a large research effort devoted to the understanding of the nitrogen localization within the carbon structure, the accurate determination of the nitrogen distribution throughout the carbon nanotube matrix remains a matter of debate, and the localization of the active phase anchorage site is still lacking. From a more general point of view, the nanoscopic localization of the nitrogen atoms within the carbon nanotube matrix will allow a better understanding of the influence of the incorporated amount and of the localization of nitrogen atoms on the physical and chemical properties of the doped-carbon nanotubes. Such understanding will be certainly helpful for the subsequent use of N-CNTs as catalyst support, in particular to establish precise structure–reactivity correlations regarding the optimization of the catalytic process.

To solve the spatial distribution of the nitrogen in such a 1D system, several experimental approaches can be in principle attempted. X-ray photoelectron spectroscopy (XPS) is one of the most employed due to its chemical selectivity; however, the obtained information is averaged on the whole specimen and is in addition mainly characteristic of the surface (few nanometers underneath). Generally, spatially solved information requires the use of imaging techniques with different selectivity. In the case of nanostructures and nanomaterials, the transmission electron microscopy (TEM)-based methods are preponderantly employed, due to the subnanometer spatial resolution as well as the multitude of physicochemical information they can provide.^{2,3} Among the different TEM modes, to obtain chemical selective information at the nanoscale, the energy dispersive X-ray and electron energy loss spectroscopies (EDX and EELS) are commonly used in combination with the scanning TEM (STEM) mode.^{3,13–16} Although both techniques, EDX and EELS, allow one in principle to map the elemental composition, it is well-known that the EELS spectroscopy is more adapted for the light elements such as carbon and nitrogen. In addition, the modern microscopes are equipped with an energy filter allowing the setup on an alternative imaging mode based on the EELS spectroscopy, that is, the energy-filtered imaging mode (EFTEM). To form an image, the electrons are selected as a function of the kinetic energy they have lost passing through the specimen. This energy loss can be related to the electron energy levels in one particular element present in the specimen, enabling thus the recording of chemical selective images. However, used in the traditional way by recording 2D images for a specific

orientation of the specimen, EFTEM imaging remains a 2D characterization tool because the projection effect induces thickness-averaged chemical information. As a consequence, for the nano-objects and nanostructures with complex 3D morphologies and random spatial distribution of components, solving chemical information by EELS or EFTEM can be very ambiguous and needs prior knowledge of the specimens. For comparison, Suenaga et al.^{17–19} have reported EELS analyses of single atoms incorporated within carbon nanostructures or forming their network structure, but the chemical mappings have been performed on very thin 3D nanostructures (single wall CNT or fullerenes) with unambiguous morphology or purely on 2D systems (graphene). Furthermore, recently Meyer et al.²⁰ have studied by HRTEM the nitrogen substitution in graphene. These works are very valuable to investigate the atomic structure of such systems. However, they are developed under very particular conditions (monolayer graphene), which are different from those that can be achieved in more complex structures as multiwalled nanotubes.

The combination of the 2D-EFTEM imaging with a tomographic approach allows one in principle to solve the chemical information at 3D in thicker carbon nanostructures specimens through the analysis of chemical selective tomographic reconstruction.^{21,22} This relatively new technique has an impressive potential because it combines the ability of the traditional electron tomography to solve information at 3D with nanoscale spatial resolution and the chemical selectivity of the EFTEM imaging. By applying EFTEM tomography at energy losses corresponding to core levels (core-loss EFTEM), several pioneering works were performed until now. On the one hand, some of these works report its first implementations in the material fields^{22,23} and the further progress in the experimental settings and data treatment,^{24,25} as well as its limitations as compared to other tomographic modes.^{26,21} On the other hand, some other works were devoted to the application of this technique for obtaining reliable chemical information at 3D: to map the calcium or phosphorus concentration in biological specimens,^{27,28} to study the 3D localization of carbon in carbonaceous nanocomposites,²⁹ to obtain information on the oxidation degree at the surface of a SiC nanograin,³⁰ to separate at nanoscale the 3D distributions of the silica and alumina within a porous grain of heterogeneous catalyst support,³¹ to solve the spatial distribution of Y₂O₃ nanoparticles within a FeAl matrix,³² and to obtain reliable chemical maps of the different components in semiconductor devices.³³ However, until now no published work reports on the determination of chemical 3D maps within thin structures such as N-CNT arches. In addition to their small sizes, they represent here small parts of a bigger object with reduced contributions to the global 2D-TEM images or EELS spectra. In such a case, to solve their chemical composition, one of the best alternatives is to combine the chemical 2D imaging at the nanoscale with the tomographic approach.

It is worth mentioning here that the application of the electron tomography to the study of carbon nanostructures is not new, with several previous works being devoted to the 3D analysis of such systems.^{34–36} However, most of them reported principally on the determination of the spatial distribution of metallic nanoparticles onto the carbon nanotubes; in this case, the contrast in classical TEM images is high enough to allow the separation of the two components by traditional TEM tomography. This is not the case for the system of interest here, where the carbon and nitrogen have close atomic numbers and

are mixed at the atomic scale, and thus the tomographic approach should be combined with the chemical selectivity to allow their distinction at 3D.

In this framework, the goal of this Article was to obtain combined information on the morphology of N-CNT and the spatial localization of the nitrogen atoms within the tubes by using the EFTEM tomography. Mapping at 3D the nitrogen distribution has a crucial importance for understanding and optimizing the electronic properties of the doped nanotubes, highlighting thus the impressive potential of this technique and in particular the high interest of such a study. For instance, when these nanotubes are used as support in catalysis, the catalytic activity of metallic particles can be influenced by the amount of N atoms inserted in the structure as well as by their spatial distribution, as their presence changes the local electron density at the surface, which in turn influences its acid–base character and catalytic activity for the metal-free catalyst application, or modifies the metal active phase dispersion and its electronic properties when used as metal catalyst support.^{37,38} In addition, the 3D characterization of N-CNTs from both chemical and morphological points of view can provide information on the mechanism of N insertion during the growth process as well. Finally, the last aim of this study is to contribute to the development of new analysis tools having several selectivities at the nanoscale, such as the EFTEM tomography, allowing one thus to characterize 3D inhomogeneous nanostructures and more specifically the correlations between their structural, chemical, and morphological characteristics. Because of their 3D character and inhomogeneous chemical composition, the highly doped N-CNTs represent ideal systems for such a methodological development and also an interesting metal-free catalyst, which could be efficiently employed in several reactions of interest in the field of off-gas purification or fine chemical. It is worth mentioning that this work concerns exclusively the 3D analysis of purified N-CNTs and not the nanocomposite made of growth catalyst and N-CNT. Although the structural characterization of the catalyst particle and of the interface with the N-CNT can provide additional information on the growth process, it does not require necessarily a 3D analysis and will be the subject of another article.

■ EXPERIMENTAL METHODS

Nitrogen-Doped Carbon Nanotube (N-CNT) Synthesis. The N-CNTs were synthesized by chemical vapor deposition (CVD) using a mixture of $C_2H_6/Ar/NH_3$ on an alumina supported iron catalyst. The iron loading was set at 20 wt %. The details of the synthesis and the catalyst preparation were already described in a previous publication.³⁹ Nitrogen source was provided by ammonia (Air liquide, 99.9996%), which was cofed into the reactant mixture. Ethane (Linde, 99.9995%) and argon (Linde, 99.99995%) were used as carbon source and carrier gas, respectively. Using the experimental design described in ref 6, the synthesis temperature was varied between 600 and 850 °C, and the ethane/ammonia concentration (defined as a volume percentage of $C_2H_6/(C_2H_6 + NH_3)$) was between 20 and 100 vol %. The as-synthesized N-CNTs were treated in a soda solution (20 wt %) at 110 °C for 24 h to dissolve residual alumina support. The solid was washed several times with deionized water until a neutral pH was reached. It was further treated with an aqua regia medium at 110 °C for 17 h to remove the residual iron catalyst following by water washing as reported previously. It is expected that these treatments could have a deep impact on the surface properties of the support due to the reactivity between the incorporated nitrogen species and the acid medium. However, these different basic and acid treatments have been necessary to obtain a final material with surface properties similar

to those of N-CNTs, which will be subsequently employed as catalyst or catalyst support to establish reliable structure–reactivity correlations. These treatments could also help to reduce the inhomogeneous distribution of the nitrogen atoms on the external surface of the nanotubes for their subsequent use in different downstream applications.

Additional Characterization Techniques (XPS, HRTEM, EELS). The XPS measurements were performed on a Multilab 2000 (Thermo Electron) spectrometer equipped with Al $K\alpha$ anode ($h\nu = 1486.6$ eV). The C1 peak fixed at $284.4(\pm 0.2)$ eV was used to correct the different XPS peaks from charging effects. All of the spectra were decomposed as summing several contributions, each of them having a Doniach–Sunjic shape and a Shirley background subtraction.

The HRTEM and EELS-STEM analyses were performed on a JEOL 2100 F electron microscope with a Cs probe corrector and a postcolumn GATAN energy filter. EELS-STEM studies have been also carried out using a FEI Titan Low-based microscope also equipped with a Cs probe corrector, working at 80 kV.

For the EELS-STEM analysis, several 1D and 2D EELS spectra were recorded for various positions of the electron beam focused probe (0.25 nm in diameter) using a convergent angle α of about 25 mrad and a collection angle β of 30 mrad.

Setup of EFTEM Tomography. The EFTEM tomographic series were recorded by using the GATAN acquisition software on the JEOL 2100 F electron microscope. Seven energy-filtered images were recorded at each tilt angle: a Zero-Loss image, three images at the K edge of C (240, 275, and 296 eV), and finally three images at the K edge of N (361, 382, and 404 eV). The slit width used to record the ZL images was 10 eV, whereas for the core-loss energy-filtered images slit widths of 30 and 20 eV were considered for C and N, respectively. The acquisition time was 2 s for the images over the C–K edge, 10 s for the images over the N–K edge, and 0.2 s for the Zero-Loss images. All of the images have a size of 512×512 pixels and were recorded using a CCD detector on which the pixel size corresponds to 0.56 nm. The seven series of energy-filtered images were obtained by varying the tilt angle from $+65^\circ$ to -65° with a tilt increment agreeing with a 3° Saxton scheme,⁴⁰ and then a total of 55 images were obtained. No visible irradiation damages were observed during the whole acquisition process (about 90 min). During the analysis, the incident electron beam density was constant for the acquisition of filtered images, which requires a specific adjustment of the illumination conditions when going from an ionization edge to the other. Furthermore, the validity of the projection is satisfied, giving that the global contribution of the diffraction contrast to the series of energy-filtered images can be considered as negligible in first approximation. In addition, the specimen thickness is constant over the whole angular range, and its value is largely below the inelastic mean free path of the electrons. Thus, multiple inelastic scattering effects are negligible, and the dynamical multiple elastic scattering is not too high.

Because of their high contrast and SNR, the standard alignment tools of the IMOD software⁴¹ (a cross-correlation algorithm followed by a fine alignment using gold fiducial markers) were used to align the Zero-Loss tilt series. A thorough work was to calculate the series of C and N 2D maps from the series of energy-filtered projections. The C and N 2D elemental images at each tilt angle were thus obtained using customized software (manuscript in preparation). First, the energy-filtered images were aligned to the corresponding Zero-Loss images. This allowed the use of the alignment parameters previously obtained for the Zero-Loss tilt series directly on the elemental projections, leading to three spatially correlated series of projections. Second, due to the poor contribution of the N chemical signal to the energy-filtered images recorded at the N–K edge, their signal-to-noise ratio (SNR) was improved by using a statistical approach (principal component analysis).^{42,43} Third, power law fitting was used to remove the background contribution, obtaining thus two series of C and N elemental images, both correlated to the ZL tilt series.

A shape-sensitive and two elemental (C and N) reconstructions have been computed using iterative approaches from the tilt series of Zero-Loss and C and N 2D elemental projections. The iterative approach has consisted of an algebraic reconstruction technique⁴⁴

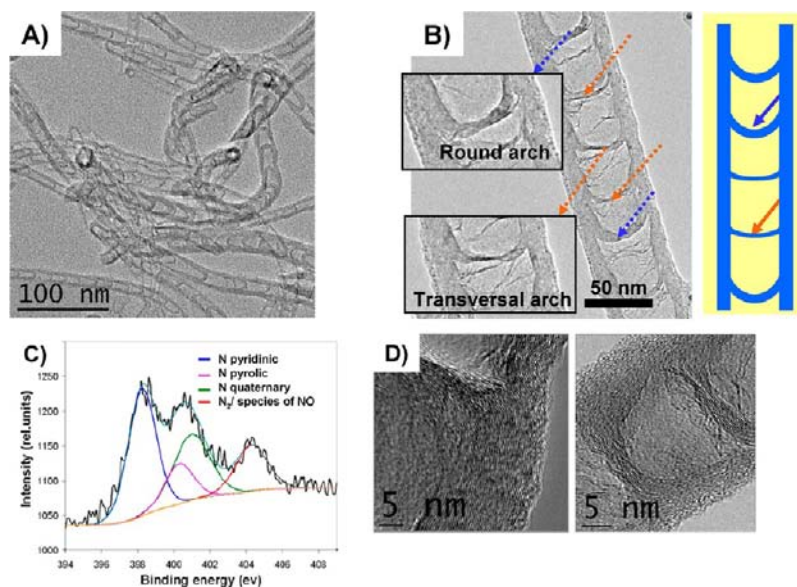


Figure 1. (A) 2D-TEM micrograph of the N-doped CNTs showing the presence of periodically arches along the tube axis. (B) Closer view of the microstructure of the tube where two kinds of arches can be observed: rounded arches with smooth curvature (indicated by blue arrows) and straight bended arches perpendicular to the external walls (orange arrows); a schematic representation of the microstructure is also presented. The dark particles visible on the carbon membrane and on the tube are gold beads (5 nm size) that are used as fiducial markers in the alignment step of the tomographic procedure. (C) XPS mean spectrum of a macroscopic assembly of N-doped CNTs taken over the N–K ionization edge; the contributions of the different configurations of the nitrogen atoms inserted within the graphitic layers are also schematized. (D) Typical HRTEM images taken on the two types of arches, illustrating the presence of a higher density of structural defects within the transversal arches (left image) as compared to the rounded ones (right image).

implemented in the TOMOJ software⁴⁵ with a number of 15 iterations. Once the three tomographic reconstructions were computed, the external borders and the internal structure of the tube were extracted from the shape-sensitive volume by using a segmentation procedure based on the gray-level intensities of the voxels. Note that the knowledge of the external shape and internal structure of the tube allows a precise determination of the voxels representing the material, simplifying thus the data segmentation process of the elemental volumes, a step difficult to realize otherwise due to their low SNR. Once the 3D structure of the tube (made of longitudinal walls and arches) was deduced, a simple selection criterion was used to attribute a given voxel to one of the two elements. This criterion is based on the direct comparison of the two intensities, voxel by voxel, which were averaged over a 3 voxel diameter sphere, to reduce the statistical noise.

The spatial resolution in the 3D elemental maps depends on several factors: the geometrical parameters of the tilt series, the accuracy of the data processing, as well as the resolution in the 2D elemental projections. In first approximation, this 3D analytical resolution can be estimated as follows: $R_{3D} = (R_{2D}^2 + R_{\text{tomo}}^2)^{1/2}$, with R_{tomo} the resolution of the tomographic approach and R_{2D} the 2D analytical resolution. The tomographic-specific resolution depends on the data collection geometry and was estimated by using the analytical relations given by Radermacher et al.⁴⁶ The 2D analytical resolution was approximated by taking into account the microscope aberrations and the experimental conditions of the acquisition process. We have deduced thus a global theoretical resolution in the 3D elemental maps of C and N of about 5 and 7 nm, respectively.

RESULTS AND DISCUSSION

To obtain reliable information on the spatial localization of the nitrogen atoms in N-CNT, we have focused our attention on the N-CNTs doped with a high amount of N (about 18 at. %), giving that this characterization tool at 3D is certainly not enough sensitive to detect concentrations of only few percent, especially if the distribution of the doping atoms is relatively homogeneous. Furthermore, as detailed in the Introduction,

several 2D studies have indicated a rather heterogeneous distribution of the N atoms within the CNT structures. Thus, in this context, it is obvious that this effect is more evident and then easier to probe for the higher nitrogen concentration. On the other hand, there is another advantage of working on these N-CNTs where a high amount of N is incorporated, which is that eventual morphological changes in the radial plane of the tube due to the nitrogen addition would be more visible.

A low magnification TEM-2D micrograph of the N-CNT doped with a high amount of nitrogen is shown in Figure 1A and shows the formation of a bamboo-like structure along the tube axis, which is typically for these doped carbon nanotubes. The presence of nitrogen incorporated within the graphitic layers was confirmed by X-ray photoelectron spectroscopy (XPS) analysis (Figure 1C). According to these measurements, several nitrogen species are present in the material, that is, nitrogen–carbon and nitrogen–oxygen species.^{47,48} Indeed, it is expected that during the growth process the nitrogen atoms are inserted within the carbon matrix by different reactions leading to a variety of nitrogen–carbon and nitrogen–oxygen species in the final sample. Note that oxygen atoms are systematically introduced into the synthesis medium as impurities in the different gases used during the course of synthesis. Arigo et al.⁴⁸ have reported a very detailed work devoted to the study by XPS of the nature of these different N–C and N–O groups formed by postsynthesis amination treatment. The first N_{1s} peak located at around 398.0 ± 0.2 eV is usually assigned to pyridine-like N atoms,⁴⁹ the second N_{1s} peak from 400.0 ± 0.2 eV could be assigned to N atoms in a pyrrole-like configuration,⁵⁰ whereas the third N_{1s} peak at 401.0 ± 0.2 eV is usually assigned to the quaternary nitrogen,⁵¹ which could be a quaternary N due to intra- or intermolecular hydrogen bonds between pyridine or aniline functions. Finally, the last N_{1s} peak located at around 404.5 ± 0.2 eV is referred to

as nitrogen–oxygen bonds. The average N-to-C atomic ratio, localized within the first tenth walls of the tube, determined by XPS is ca. 18 at. %, which is among the highest doping concentrations reported up to now. As XPS analyses provide chemical information from the surface atoms (<4–5 nm in depth or tenth walls in average), elemental microanalysis measurements have been also performed to determine the global atomic percentage of nitrogen within the analyzed tubes. The results were similar, showing that the nitrogen atoms are distributed quite homogeneously in the radial plane of the tube. Conventional and high-resolution TEM images (Figure 1B and D) allow us to observe the presence of different microstructures of the graphene sheets within the N-CNT arches, that is, continuous curvature arch and perpendicular arch (see the schematic representation in Figure 1). The last one presents an amorphous curled zone, which could be attributed to the structural disturbing of the graphene sheet by nitrogen incorporation. A statistical analysis performed on several representative highly doped N-CNTs allowed us to observe that the longitudinal distance between two successive arches does not depend necessarily on the type of arches and that the corresponding mean value is about 50 nm. A simple analysis of the classical TEM images showed also that the relative number of the perpendicular arches is about 75% from the total number and that they are systematically thinner as compared to the rounded ones (see detailed discussion below). It is worth noting that this is not the case for N-CNTs with low nitrogen content, which present generally a unique type of arch, that is, rounded arches.⁵² Such results indicate that the perpendicular arches are probably linked with the high nitrogen concentrations in the nanotube.

To obtain primary information on the localization of the N atoms in the N-CNTs, EELS-STEM analysis has been performed in a first step. By using this chemical selective mode, previous results have strongly suggested that nitrogen atoms are preferentially situated in the inner walls of the tube. Such results have already been reported by other groups in the literature.^{53,54} The CNTs' growth mechanism generally proceeds via adsorption and decomposition of the gaseous hydrocarbon species followed by carbon atoms incorporation. It is generally assumed that the first carbon walls are nucleated via surface carbon diffusion on the metal catalyst while the subsurface diffusion leads to the formation of the inner walls of the nanotube.^{55,56} Rinaldi et al.⁵⁷ have reported that in the case of nickel catalyst the carbon migration to the subsurface is favored for both Ni(111) and Ni(100) facets. Similar conclusions have also been reported by Hofmann et al.,⁵⁵ who demonstrated that subsurface diffusion requires less energy than surface or bulk diffusion as well as that subsurface diffusion is favored over bulk diffusion due to the migration of the nickel atoms upward to the surface. The growth mechanism and, as a consequence, the localization of the nitrogen atoms versus the carbon atoms in the final N-CNTs will also be affected by the lower solubility of nitrogen atoms inside the metal matrix, which was used as growth catalyst.^{5,15} According to these hypotheses, one should expect that the first walls of the as-synthesized N-CNTs will be carbon-rich, due to the faster formation of FeC_x versus FeN_x, while the inner walls that grow later via the subsurface diffusion on the FeN_x stable phase, after N-saturation, will be nitrogen-rich. The theoretical results reported by Sumpter et al.⁵⁴ indicate also that a ring of N is preferentially localized closer to the end-cap than in the bulk, suggesting thus that the presence of nitrogen atoms induces the

closure of the tube and leads to the formation of periodical compartments along the tube axis. The same authors have also reported that nitrogen prefers to be localized at the tube edge as it becomes unstable far inside the carbon hexagonal lattice. Therefore, once the tube edge becomes N-saturated, the growth process is interrupted unless part of the nitrogen atoms is removed and replaced by carbon or the structure is stabilized by the presence of defects induced by the closure of graphitic planes to form a cap. This process and the previous one regarding the high tendency of the N ring to be close to the tube's cap could be both responsible for the formation of periodical thin caps with high nitrogen concentration.

In this general framework related to the determination of the localization of N atoms within the graphitic structure, classical 2D EELS-STEM analyses have been performed on different N-CNTs investigated in this work, doped with a small and high amount of nitrogen (see the Supporting Information, SI 1 and SI 2). As expected, in the tubes with a small amount of N (3 at. %), solving the distribution of the doping atoms is not an easy task, even at two dimensions. In contrary, on the highly doped N-CNT, the analyses performed either in line-scan mode or in 2D mapping^{43,58} suggest that the nitrogen is present homogeneously over the whole structure of the tube (Figure 2A). However, some more localized investigations have shown that the nitrogen concentration can vary considerably from one area to another, being higher inside the areas where arches are present (Figure 2C), which could be due to the closure mechanism described above. As a matter of fact, from the analysis of the spectrum-imaging of Figure 2A and B, we can observe that the amount of N can be almost 20% (area 3, middle of the arch) and only 8% in the region close to it (area 0, inside of one of the compartments). It can be observed in Figure 2C. The fine structure near (ELNES) of the C–K edge consists of a sharp π^* peak at ~ 285 eV and a σ^* band starting at ~ 292 eV. The ELNES analyses of the different EEL spectra extracted from the spectrum-imaging of the Figure 2B show that these signatures are typical of graphitic network, sp² hybridization of the C atoms, but also pointed out the existence of other different C configurations in these different positions/areas within this analyzed region: from amorphous-like or less organized carbon⁵⁹ (area 3 – middle of the arch) to more graphitic ones as is the case of area 0 (in the compartment); see Figure 2D and mainly Figure 2E, which is a zoom of the C–K edge. Thus, this indicates that there is some correlation between the N content and the density of defects or crystallinity/graphitization degree. A detailed analysis of the N–K edge (Figure 2F) shows two different regions/bands: one corresponding to the π^* contribution (397–403 eV) and the other to the σ^* contribution (405–420 eV). The nature of these bands can be analyzed with reference to previous studies performed on CN_x materials, either in CN_x films or on CN_x-MWNTs.^{2–5,13–16} The triangular peak at ~ 405 eV present in the spectrum is characteristic of the σ^* band in CN_x-MWNTs, displaying a sp² kind of bonding.^{2–5,15,16} On the other hand, from the π^* region, one can deduce the coexistence of two different atomic configurations for the N atoms: the graphitic one (~ 401 eV) and the pyridine-like one (peak at ~ 398 eV).^{2–5,15} However, it is worth mentioning that the correlation commonly made with pyridine-like and graphitic-like configurations is only indicative of the fact that N displays two kinds of chemical bonding when embedded into a carbon wall.^{2–5} Further theoretical and experimental studies should be carried out to correlate experimental data with accurate theoretical

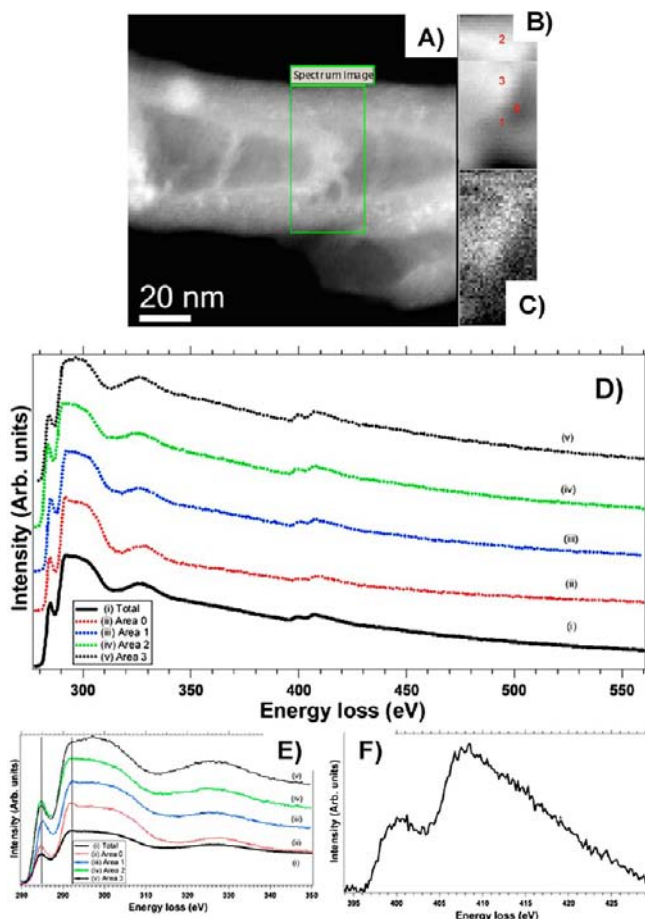


Figure 2. EELS mapping on a typical area of a highly doped N-CNT. (A) Global HAADF-STEM view of the analyzed N-CNT. (B) HAADF-STEM image of the EELS analyzed area corresponding to the green rectangle from (A). The positions chosen for a more detailed EELS analysis are marked in red. (C) N map extracted from a general spectrum-imaging recorded on the K-edge of nitrogen after the background removal. (D) The individual EELS spectra, after the background removal, corresponding to the positions marked in (B). (E,F) Zoom on the EELS spectra at C and N K edges, respectively (in the case of N K edge, the curve corresponds to the addition of the spectra). The N concentration obtained by the quantification of the spectra which correspond to the different positions are: 8.3% (Area 0), 13.8% (Area 1), 16.5% (Area 2) and 19.7% (Area 3).

calculations.^{2–5,15} It is obvious that the insertion of such a high concentration of N within the graphitic planes is at the origin of the high density of defects observed in the high-resolution TEM images. Note that the presence of molecular nitrogen species was also occasionally evidenced in some compartments of the tube (see the Supporting Information, SI 3).

To summarize the spectroscopic 2D studies, although the nitrogen atoms seem to be preferentially localized on the arches, the obtained results were not sufficient relevant to solve their exact spatial distribution (in particular, a difference in the doping degree between the transversal and rounded arches) and to correlate the presence of nitrogen with some possible changes in the tube morphology, which are not visible in a simple TEM image.

From a more general point of view, as explained in the Introduction, the relatively high depth-of-view in TEM and STEM modes on the studied object gives rise to thickness-integrated information in 2D images or spectra. As a result, the

localization by 2D EFTEM or EELS of the nitrogen atoms within the N-doped CNT structure and more particularly in the two types of arches is very difficult. That necessitates techniques that are able to separate the two elements in three dimensions with a nanometer resolution and, if possible, to provide images with an increased SNR ratio with respect to the 2D chemical images, as is the case of EFTEM tomography.

In this context, tomographic experiments in the EFTEM mode were carried out to obtain simultaneously nanoscale 3D information on the localization of the N atoms and on the tube morphology in cross-section. The mean EELS spectrum of the chosen area is shown in Figure 3A and illustrates the experimental parameters (positions and widths of the energy windows) used for the acquisition of the filtered images at the K-edge of N. Figure 3B presents the set of images recorded at 0° tilt angle, the Zero-Loss one followed by three energy-filtered images at the C- and N-K edges, respectively. By using the signal extraction procedure given in the experimental section, series of 2D elemental maps were calculated for the carbon and nitrogen. Three typical elemental 2D maps extracted from the computed tilt series, together with the corresponding Zero-Loss images, are given in Figure 3C. It is worth mentioning that, as there was not specimen drift during the acquisition of the seven images at a given tilt angles, the three tilt series (ZL and those of C and N) are spatially correlated. By applying the reconstruction algorithm, they give rise to three spatially correlated volumes, the sensitive-shape one (obtained from the Zero-Loss recording) and the two elemental reconstructions (from the two series of 2D elemental maps).

Once the three volume reconstructions were calculated, a slice-by-slice analysis was performed in a combined manner. Three longitudinal slices containing the main axis of the tube extracted from the three individual reconstructions are illustrated in Figure 4. The equivalent slice through the C-to-N relative 3D map that was obtained by superimposing the two elemental ones is also presented in the same figure, with C in red and N in green. This 3D representation of the chosen N-doped CNT gives rise to a global view of the nitrogen incorporation within the carbon network, which has never been observed so far. A quick qualitative analysis consisting of a direct visualization of the 3D relative reconstruction slice-by-slice allowed us to highlight that for the perpendicular arches, the green component, nitrogen, is much more pronounced than that for the rounded ones. Tomography allows one to solve the signal of interest at 3D, which indicates that the nitrogen concentration is higher within the perpendicular arches as compared to the arches with smooth curvature. It is worth mentioning here that a quantification of the N amount in the two arches would be unreasonable, given the poor signal-to-noise ratio in the elemental reconstructions. However, the qualitative difference in C-to-N within the two arches agrees with the results obtained by high-resolution TEM, which have suggested that the transversal arches contain a high density of structural defects and consequently more nitrogen as compared to the rounded one (Figure 1D). A simple microstructural model that could explain this crystallographic difference consists of the presence of less graphitized zones across the curvature in the perpendicular arches and continuous bended graphene sheets for smooth curvature arches. This crystallographic difference between the two types of arches combined with their morphological and chemical characteristics deduced by EFTEM tomography allowed us to tentatively propose a

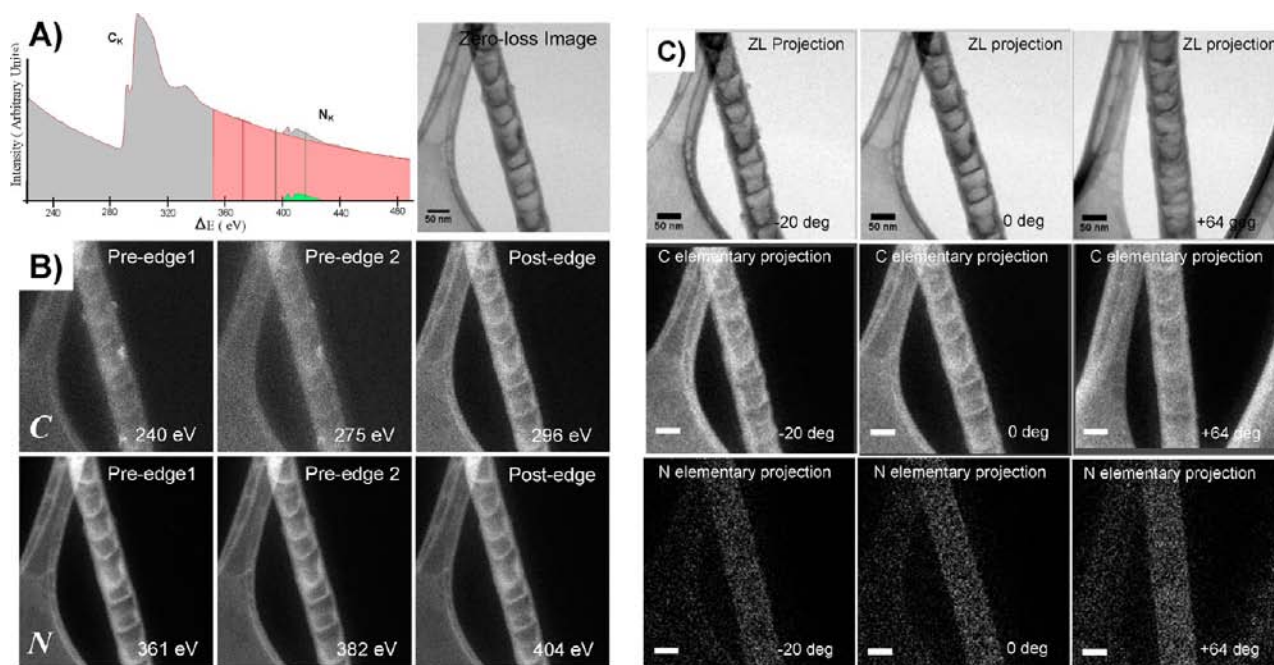


Figure 3. (A) Mean EELS spectrum taken on the studied area of the N-doped carbon nanotube. The presence of two types of arches (i.e., transverses and rounded ones), which is typical for the highly doped CNTs, can be observed. (B) The series of seven images acquired at the 0° tilt angle: Zero-Loss image, three energy-filtered images (generally called “pre-edge 1”, “pre-edge 2”, and “post-edge”) at the C–K edge, and three corresponding to the N–K edge. (C) Three typical images extracted for the tilt angles of 64° , 0° , and -20° from the spatially correlated tilt series of as-recorded Zero-Loss images (top) and 2D elemental maps of C (middle) and N (bottom) calculated by the decomposition method described in the experimental section using as input the series of EFTEM images. One can easily observe that the SNR is considerably lower in the 2D elemental maps of N as compared to that of C.

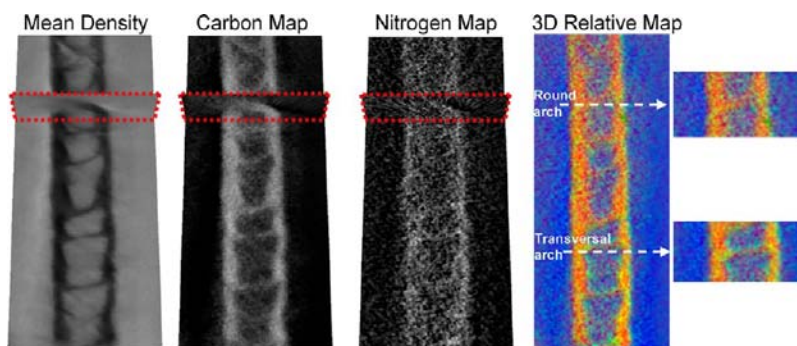


Figure 4. Typical longitudinal slices extracted at the same depth and orientation from the shape-sensitive reconstruction (left), C and N 3D elemental maps (middle), and C-to-N 3D relative map (right). The last one was obtained by superimposing the two elemental 3D maps with different colors, nitrogen in green and carbon in red. Note that the two types of arches are present within the analyzed area.

mechanism for the N insertion within the highly doped N-CNTs. First, as the distance between two arches is almost the same along the tube and the rounded arches are thicker and with a lower local nitrogen concentration, one can suppose that the total N amounts incorporated within the two arches are similar, that is, the N amount to be incorporated in an arch for a given distance along the tube axis. During the growth process, if the density of structural defects at a position where an arch tend to form is high, the result is a perpendicular arch that can incorporate more nitrogen in a small thickness. However, if the density of defects is smaller, rounded arches are formed, which incorporate less nitrogen for a given thickness and are consequently thicker. Another possible explanation of such difference in the arches' thickness could be the periodical change in catalyst nature between FeC_x and FeN_x during the growth process. This systematic change could lead also to the

formation of caps or arches with alternate nitrogen-rich and carbon-rich compositions per arch volume. In the case of nitrogen-rich arches, the high tendency of nitrogen-rich structures to favor the closure of the graphitic planes could induce the formation of thinner arches, whereas for the carbon-rich arches the time for obtaining nitrogen-saturated edge is longer, leading thus to the formation of thicker arches as observed above.

The most striking finding was obtained by analyzing the tomographic reconstructions in cross-section. Some representative transversal slices extracted from the volume reconstructions at the positions of transversal and rounded arches are shown in Figure 5. Once again, one can observe that the slices taken at the transversal arches have a green component more pronounced than those extracted on the rounded arches, indicating thus the presence of higher nitrogen concentration.

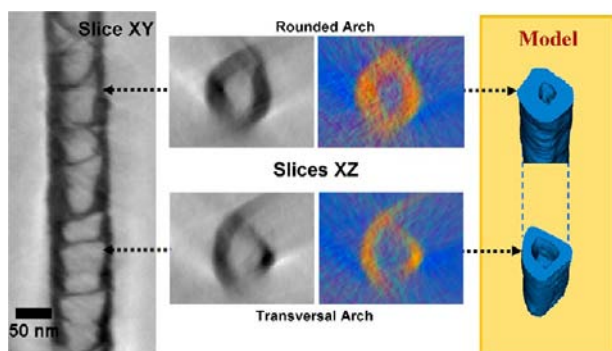


Figure 5. Combined morphological and chemical analysis of the highly doped N-CNT in cross-section. Left: Longitudinal slice extracted from the mean-density (ZL) tomographic reconstruction, which contains the longitudinal axis of the tube. Middle: Two transversal sections through the 3D mean-density and chemical relative (C-to-N) reconstructions, extracted at the positions indicated by the two arrows. Right: Cross-sectional views by the 3D model of the analyzed tube, which illustrate better its morphology at the considered positions.

More surprisingly, one can observe that at the positions where a transversal arch is present, the tube has a triangular section in cross-section instead of a circular one as is the case for rounded arches. This morphological change is certainly induced by the high amount of nitrogen atoms incorporated within the graphitic network. Indeed, the highest concentration of N (associated to the practically green voxels) seems to be present where the circular shape of the tube in cross-section is the most disturbed. To confirm that such morphological change, that is, circular to triangular morphology, is not an artifact reconstruction, several high-resolution TEM analyses were performed on the sections of N-CNTs slices obtained by using the ultramicrotome technique (see the Supporting Information, SI 4). On some of these sections, triangular shapes can be observed, showing that the triangularisation effect is well present and not a simple artifact of analysis.

All of these findings suggest that the presence of nitrogen induces a microstructure change of the graphene sheet leading to a more bended structure as compared to that of pure nanotubes. This is in agreement with some theoretical calculations performed by Kutana et al.⁶⁰ (see the Supporting Information, SI 5), which has shown that the insertion of the nitrogen atoms in the graphitic structure of carbon nanotubes can induce the tube triangularisation in cross-section. Another possible explanation of the as-illustrated morphological change of the arches within the tube could be the faceting of the growth catalyst particles during the synthesis of N-CNTs. In this context, the work published by Rinaldi et al.⁵⁷ reports on the effect of carbon incorporation into nickel active phase, which leads to a drastic modification of the electronic structure of the Ni surface, changing thus the catalytic activity of the Ni/NiC_x particles that are responsible for the subsequent growth process. Related to our work, they observe that the carbon incorporation induces a complete reconstruction of the Ni particles, which become prismatic after the carbon dissolution in their subsurface area. In a similar way, iron nanoparticles could also undergo structural or morphological modifications induced by the incorporation of nitrogen species at the beginning of the synthesis process. Such modifications could lead to a change in the surface energy of particles followed in certain cases by a surface reconstruction of the catalyst itself.

The presence of faceted particles instead of round-shaped ones could influence considerably the carbon dissolution and rejection processes, which in turn modify the shapes of arches along the growth process. In our case, it is expected that the presence of iron carbide at the surface is at the origin of the formation of thick carbon-rich rounded arches, while the iron nitride is responsible for the growth of thin triangular arches with nitrogen-rich composition. Alternatively, the incorporation of carbon atoms into the iron nanoparticles leads generally to the formation of a liquid-like phase, which is even more susceptible to undergo morphological changes as a function of the amounts of incorporated carbon or nitrogen atoms. Such effect could also considerably influence the microstructure and the morphology of the as-synthesized nitrogen-doped carbon nanotubes as well.

CONCLUSIONS

In summary, by combining EFTEM imaging with tomographic approach in electron microscopy, we have obtained correlated 3D information, at a nanoscale, on the morphology and spatial distribution of the nitrogen atoms within nitrogen-doped carbon nanotubes. A detailed analysis of the elemental volumes of carbon and nitrogen has indicated that the nitrogen is preferentially incorporated inside the transversal bended arches inside the nanotube structure, whereas the curled arches have a relatively low nitrogen incorporation. Additionally, the present work allowed us to confirm the previous hypothesis, which indirectly relates the presence of a high nitrogen amount to a microstructural change of the N-CNTs in cross-section: we have observed that in the high concentration nitrogen areas, the circular shape of the tube is disturbed and it is transformed to a prismatic structure. The results obtained indicate that this analytical technique is powerful for solving the spatial distribution of the different constituents of the material of interest with nanoscale resolution, which could be extremely helpful for the advanced characterization of a large panel of materials in several domains of applications. For instance, in the field of heterogeneous catalysis, the present technique allows one to get access to the chemical distribution of the different materials forming the catalyst and to correlate such chemical distribution with the catalytic activity to build up a correlation between the chemical structure and the reactivity of the catalyst. Such correlation is extremely helpful for developing new catalysts with optimized activity and stability.

ASSOCIATED CONTENT

Supporting Information

SI1 and SI2: 2D STEM-EELS analysis of 4% and 18% nitrogen-doped carbon nanotubes. SI 3: EELS analysis carried out for evidencing the presence of molecular nitrogen. SI4: HRTEM images of cross-sectional slices obtained by ultramicrotome evidencing the triangularization of the tube morphology. SI5: Overview on the theoretical calculations of Kutana et al. This material is available free of charge via the Internet at <http://pubs.acs.org>.

AUTHOR INFORMATION

Corresponding Author

lenuta.florea@ipcms.u-strasbg.fr

Notes

The authors declare no competing financial interest.

■ ACKNOWLEDGMENTS

I.F. acknowledges financial support from the Région Alsace for its Ph.D. grant.

■ REFERENCES

- (1) Yu, D.; Nagelli, E.; Du, F.; Dai, L. *J. Phys. Chem. Lett.* **2010**, *1*, 2165–2173.
- (2) Arenal, R.; Blase, X.; Loiseau, A. *Adv. Phys.* **2010**, *59*, 101.
- (3) Ayala, P.; Arenal, R.; Rubio, A.; Loiseau, A.; Pichler, T. *Rev. Mod. Phys.* **2010**, *82*, 1843.
- (4) Ayala, P.; Arenal, R.; Rummeli, M.; Rubio, A.; Pichler, T. *Carbon* **2010**, *48*, 575.
- (5) Ewels, C. P.; Glerup, M. *J. Nanosci. Nanotechnol.* **2005**, *5*, 1345.
- (6) Chizari, K.; Janowska, I.; Houllé, M.; Florea, I.; Ersen, O.; Romero, T.; Bernhardt, P.; Ledoux, M. J.; Pham-Huu, C. *Appl. Catal., A* **2010**, *380*, 72–80.
- (7) Van Dommele, S.; De Jong, K. P.; Bitter, J. H. *Chem. Commun.* **2006**, 4859–4861.
- (8) Su, D. S.; Zhang, J.; Frank, B.; Thomas, A.; Wang, X.; Paraknowitsch, J.; Schlögl, R. *ChemSusChem* **2010**, *3*, 169–180.
- (9) Amadou, J.; Chizari, K.; Houllé, M.; Janowska, I.; Ersen, O.; Bégin, D.; Pham-Huu, C. *Catal. Today* **2008**, *138*, 62–68.
- (10) Ma, Y.; Sun, L.; Huang, W.; Zhang, L.; Zhao, J.; Fan, Q.; Huang, W. *J. Phys. Chem. C* **2011**, *115*, 24592–24597.
- (11) Feng, L.; Yan, Y.; Chen, Y.; Wang, L. *Energy Environ. Sci.* **2011**, *4*, 1892–1899.
- (12) Chizari, K.; Deneuve, A.; Ersen, O.; Florea, I.; Liu, Y.; Edouard, D.; Janowska, I.; Bégin, D.; Pham-Huu, C. *ChemSusChem* **2012**, *5*, 102–108.
- (13) Stephan, O.; Colliex, C.; Hug, G.; Hsu, W. K.; Kroto, H. W.; Walton, D. R. M. *Eur. Phys. J. B* **2001**, *22*, 117.
- (14) Glerup, M.; Castignolles, M.; Holzinger, M.; Hug, G.; Loiseau, A.; Bernier, P. *Chem. Commun.* **2003**, *20*, 2542.
- (15) Lin, H.; Arenal, R.; Enouz, S.; Stephan, O.; Loiseau, A. *J. Phys. Chem. C* **2009**, *113*, 9509.
- (16) Susi, T.; Kaskela, A.; Zhu, Z.; Ayala, P.; Arenal, R.; Tian, Y.; Laiho, P.; Mali, J.; Nasibulin, A. G.; Jiang, H.; Jiang, T.; Lanzani, G.; Stephan, O.; Laasonen, K.; Pichler, T.; Loiseau, A.; Kauppinen, E. I. *Chem. Mater.* **2001**, *23*, 2201.
- (17) Suenaga, K.; Tencé, M.; Morry, C.; Colliex, C.; Kato, H.; Okazaki, T.; Shinohara, H.; Hirahara, K.; Bandow, S.; Iijima, S. *Science* **2000**, *290*, 2280–2280.
- (18) Suenaga, K.; Kosino, M. *Nature* **2010**, *468*, 1088–1090.
- (19) Guan, L.; Suenaga, K.; Shi, Z.; Gu, Z.; Iijima, S. *Phys. Rev. Lett.* **2005**, *94*, 045502.
- (20) Meyer, J. K.; Kurasch, S.; Park, H. J.; Skakalova, V.; Künzel, D.; Groß, D.; Chuvilin, A.; Algara-Siller, G.; Roth, S.; Iwasaki, T.; Starke, U.; Smet, J. H.; Kaiser, U. *Nat. Mater.* **2011**, *10*, 209–215.
- (21) Möbus, G.; Doole, R. C.; Inkson, B. J. *Ultramicroscopy* **2003**, *96*, 433–451.
- (22) Midgley, P. A.; Weyland, M. *Ultramicroscopy* **2003**, *96*, 413–431.
- (23) Midgley, P. A.; Weyland, M.; Yates, T.; Tong, J.; Dunin-Borkowski, R. E.; Thomas, J. M. *Microsc. Microanal.* **2004**, *10*, 148–149.
- (24) Jin-Phillipp, N. Y.; Koch, C. T.; vanAken, P. A. *Ultramicroscopy* **2011**, *111*, 1255–1261.
- (25) Midgley, P. A.; Dunin-Borkowski, R. E. *Nat. Mater.* **2009**, *8*, 271–280.
- (26) Goris, B.; Bals, S.; Vanden Broek, W.; Verbeeck, J.; Van Tendeloo, G. *Ultramicroscopy* **2011**, *111*, 1262–1267.
- (27) Leapmann, R. D.; Kocsis, E.; Zhang, G.; Talbot, T. L.; Laquerriere, P. *Ultramicroscopy* **2004**, *100*, 115–125.
- (28) Aronova, M. A.; Kim, Y. C.; Harmon, R.; Sousa, A. A.; Zhang, G.; Leapman, R. D. *J. Struct. Biol.* **2007**, *160*, 35–48.
- (29) Gass, M. H.; Koziol, K. K. K.; Windle, A. H.; Midgley, P. A. *Nano Lett.* **2006**, *6*, 376–379.
- (30) Florea, I.; Ersen, O.; Hirlimann, C.; Roiban, L.; Deneuve, A.; Houllé, M.; Janowska, I.; Nguyen, P.; Pham, C.; Pham-Huu, C. *Nanoscale* **2010**, *2*, 2668–2678.
- (31) Roiban, L.; Sorbier, L.; Pichon, C.; Bayle-Guillemaud, P.; Werckmann, J.; Drillon, M.; Ersen, O. *Microsc. Microanal.* **2012**, DOI: 10.1017/S143192761200116X.
- (32) Möbus, G.; Inkson, B. J. *Appl. Phys. Lett.* **2001**, *79*, 1369–1371.
- (33) Jarausch, K.; Thomas, P.; Leonard, D. N.; Twisten, R.; Booth, C. R. *Ultramicroscopy* **2009**, *109*, 326–337.
- (34) Ersen, O.; Werckmann, J.; Houllé, M.; Ledoux, M. J.; Pham-Huu, C. *Nano Lett.* **2007**, *7*, 1898–1907.
- (35) Tessonnier, J. P.; Ersen, O.; Weinberg, G.; Pham-Huu, C.; Su, D. S.; Schlogl, R. *ACS Nano* **2009**, *3*, 2081–2089.
- (36) Casteljos, E.; Debouttière, P.-J.; Roiban, L.; Solhy, A.; Martinez, V.; Kihn, Y.; Ersen, O.; Philippot, K.; Chaudret, B.; Serp, P. *Angew. Chem.* **2009**, *121*, 2567–2571.
- (37) Chan-Thaw, C. E.; Villa, A.; Katekomol, P.; Su, D.; Thomas, A.; Prati, L. *Nano Lett.* **2010**, *10*, 537–541.
- (38) Prati, L.; Villa, A.; Chan-Thaw, C. E.; Arrigo, R.; Wang, D.; Sub, D. S. *Faraday Discuss.* **2011**, *152*, 353–365.
- (39) Gulino, G.; Vieira, R.; Amadou, J.; Nguyen, P.; Ledoux, M. J.; Galvagno, S.; Centi, G.; Pham-Huu, C. *Appl. Catal., A* **2008**, *279*, 89–97.
- (40) Saxton, W.; Baumeister, W.; Hahn, M. *Ultramicroscopy* **1984**, *13*, 57–70.
- (41) Mastronarde, D. N. *J. Struct. Biol.* **1997**, *120*, 343–352.
- (42) Trebbia, P.; Bonnet, N. *Ultramicroscopy* **1990**, *34*, 165–78.
- (43) Arenal, R.; De la Pena, F.; Stephan, O.; Walls, M.; Tence, M.; Loiseau, A.; Colliex, C. *Ultramicroscopy* **2008**, *109*, 32.
- (44) Gordon, R.; Bender, R.; Herman, G. T. *J. Theor. Biol.* **1970**, *24*, 471–481.
- (45) Messaoudi, C.; Boudier, T.; Sanchez Sorzano, C. O.; Marco, S. *Bioinformatics* **2007**, *6*, 288.
- (46) Radermacher, M. *Scanning Microsc.* **1997**, 171–177.
- (47) Kundu, S.; Xia, W.; Busser, W.; Becker, M.; Schmidt, D. A.; Havenith, M.; Muhler, M. *Phys. Chem. Chem. Phys.* **2010**, *12*, 4351–4359.
- (48) Arrigo, R.; Havecker, M.; Wrabetz, S.; Blume, R.; Lerch, M.; McGregor, J.; Parrott, E. P. J.; Zeitler, J. A.; Gladden, L. F.; Knop-Gericke, A.; Schlogl, R.; Su, D. S. *J. Am. Chem. Soc.* **2010**, *132*, 9616–9630.
- (49) Boudou, J. P.; Chehimi, M.; Broniek, E.; Siemieniewska, T. *Carbon* **2003**, *41*, 1999–2007.
- (50) Staczyk, K.; Piwowarska, Z.; Witkowski, S. *Carbon* **1995**, *33*, 1383–1392.
- (51) Kelemen, S. R.; Gorbaty, M. L.; Kwiatek, P. J. *Energy Fuels* **1994**, *8*, 896–906.
- (52) Chizari, K.; Janowska, I.; Houllé, M.; Florea, I.; Ersen, O.; Romero, T.; Bernhardt, P.; Ledoux, M. J.; Pham-Huu, C. *Appl. Catal., A* **2010**, *380*, 72–80.
- (53) Trasobares, S.; Stephan, O.; Colliex, C.; Hsu, W. K.; Kroto, H. W.; Walton, D. R. W. *J. Chem. Phys.* **2002**, *116*, 8966.
- (54) Sumpter, B. G.; Meunier, V.; Romo-Herrera, J. M.; Cruz-Silva, E.; Cullen, D. A.; Terrones, H.; Smith, D. J.; Terrones, M. *ACS Nano* **2007**, *4*, 369–375.
- (55) Hofmann, S.; Csanyi, G.; Ferrari, A. C.; Payne, M. C.; Robertson, J. *Phys. Rev. Lett.* **2005**, *95*, 036101.
- (56) Tessonnier, J. P.; Su, D. S. *ChemSusChem* **2011**, *4*, 824–847.
- (57) Rinaldi, A.; Tessonnier, J. P.; Schuster, M. E.; Blume, R.; Girgsdies, F.; Zhang, Q.; Jacob, T.; Abd Hamid, S. B.; Su, D. S.; Schlögl, R. *Angew. Chem., Int. Ed.* **2011**, *50*, 3313–3317.
- (58) Jeanguillaume, C.; Colliex, C. *Ultramicroscopy* **1989**, *28*, 252.
- (59) Liu, A. C. Y.; Arenal, R.; Miller, D. J.; Chen, X.; Johnson, J. A.; Eryilmaz, O. L.; Erdemir, A.; Woodford, J. B. *Phys. Rev. B* **2007**, *75*, 205402.
- (60) Kutana, A.; Giapis, K. P. *J. Phys. Chem. C* **2009**, *113*, 14721–14726.